CHAPTER 8

Solid-State Transformations

EUTECTOID AND PERITECTOID transformation are classified as solid-state invariant transformations. Invariant transformations are isothermal reversible reactions that occur at an invariant point on the phase diagram of an alloy, where the initial (parent) phase may be either a liquid or a crystalline solid. Solid-state invariant reactions are a category of heterogeneous phase transformations that involve moving reaction boundaries and phase separation. Invariant transformations differ from precipitation reactions in that all reaction products from an invariant transformation have a different crystal structure than that of the parent phase. In contrast, solid-state transformation from a discontinuous precipitation involves the generation of new second phase within a matrix that has the same crystal structure as the parent phase in precipitation structures.

As in the case of invariant reactions during solidification, important solid-state transformations from invariant reactions are of three types:

- *Eutectoid transformation,* where a solid solution converts into two or more intimately mixed solids with different crystal structures than that of the parent phase. The number of solid phases formed equals the number of components in the system. The reaction is:

$$\text{Solid } \gamma \rightarrow \text{Solid } \alpha + \text{Solid } \beta$$

- *Peritectoid transformation,* where two solid phases of a binary alloy transform into one phase on cooling. Peritectoid reactions are similar to peritectic reactions, except that one of the initial phases is liquid in a peritectic reaction. As in all invariant reactions, peritectoid reactions are reversible; that is, the $\alpha + \beta$ are recovered on heating the reaction product, γ. The reaction is:

$$\text{Solid } \alpha + \text{Solid } \beta \rightarrow \text{Solid } \gamma$$

- *Monotectoid transformations,* where cooling or heating of a solid solution completely converts it into a solid solution with a different crystal structure (Fig. 8.1). A monotectoid reaction differs from a eutectoid reaction in that only one reaction phase is produced. The reaction is:

$$\text{Solid } \alpha \rightarrow \text{Solid } \gamma$$

The monotectoid reaction is not prevalent in commercial alloys and is not discussed further in this chapter. This chapter focuses primarily on structures from eutectoid transformations with emphasis on the classic iron-carbon system of steel. Peritectoid phase equilibria also are very common in several binary systems but are only briefly reviewed.

Solid-state reactions differ in two important aspects from liquid reactions in the manner in which they attain the equilibrium conditions predicted by the phase diagram. Solid-state reactions occur much more slowly, are subject to greater undercooling, and rarely attain true equilibrium conditions. Solid phases consist of atoms arranged in certain crystal structures, and new solid phases forming out of an existing solid phase tend to take definite positions with respect to the existing crystal structure. In other words, the crystal structure of the new phase has a definite orientation relationship to the crystal structure of the phase from which it formed.

8.1 Iron-Carbon Eutectoid Reaction

Most carbon steels contain up to 1.5% C, while cast irons normally contain 2 to 4% C. As discussed in Chapter 2, "Solid Solutions and Phase Transformation," in this book, iron is allotropic and changes its crystalline

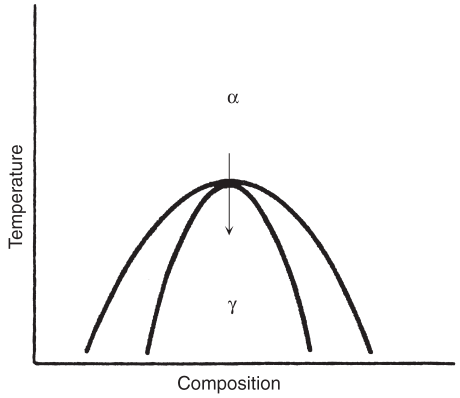

Fig. 8.1 Schematic phase diagram of a monotectoid reaction. Source: Ref 8.1

structure on heating or cooling. When pure iron solidifies on cooling from its melting point of 1540 °C (2800 °F), it assumes a body-centered cubic (bcc) structure designated as δ-ferrite. On further cooling between 1395 and 910 °C (2541 and 1673 °F), it has a face-centered cubic (fcc) structure called austenite, designated as γ. Below 910 °C (1673 °F), it again has a bcc crystal structure called ferrite, designated as α.

The fact that steel can be hardened is a direct result of the eutectoid reaction in iron-carbon alloys. Just as a eutectic reaction involves the decomposition of a liquid solution, a eutectoid reaction involves the decomposition of solid solution into two other solid phases. The iron-carbide phase diagram is shown in Fig. 8.2. The composition only extends to 6.70% C; at this composition the intermediate compound iron carbide, or cementite (Fe_3C), is formed, represented by the vertical line on the right hand side of the diagram. Because all steels and cast irons have carbon contents less than 6.70%, the remainder of the diagram with 6.7 to 100% C is of no engineering interest. Cementite is a hard and brittle intermetallic compound with an orthorhombic crystalline structure.

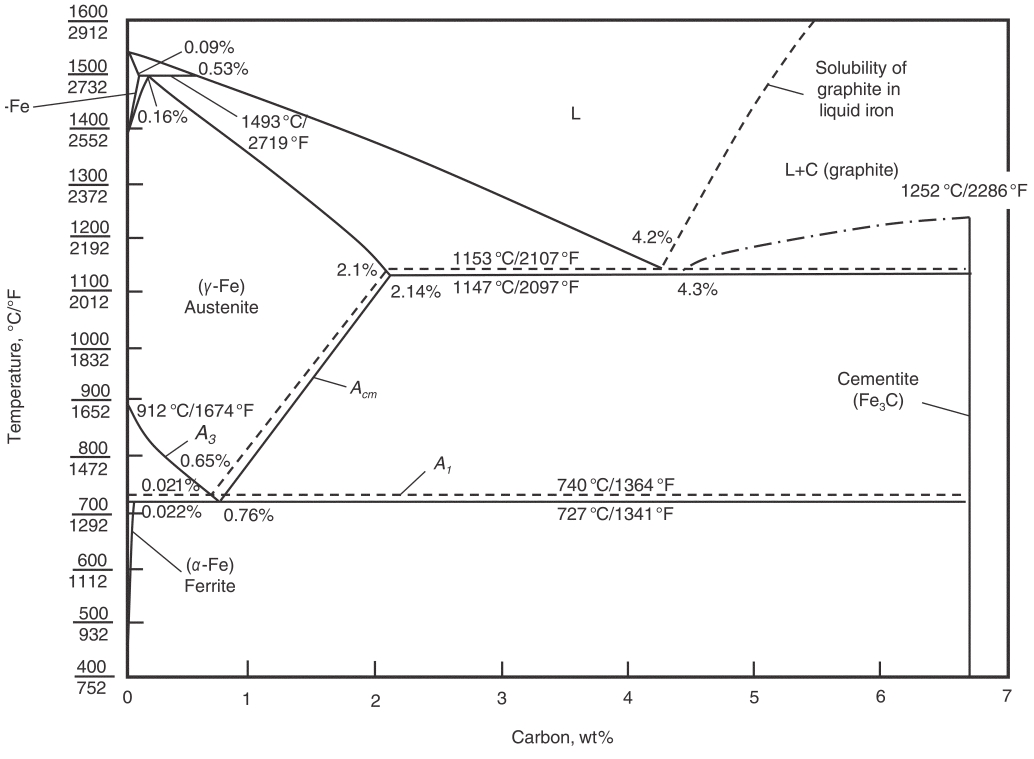

Fig. 8.2 The Fe-Fe_3C diagram. Solid lines indicate Fe-Fe_3C diagram; dashed lines indicate iron-graphite diagram. Source: Ref 8.2 as published in Ref 8.3

Carbon forms a series of solid solutions with iron, as indicated by the δ, γ, and α fields. However, carbon has very limited solubility in iron. The maximum solubility of carbon in ferrite is only approximately 0.022 wt% at 171 °C (340 °F) that increases to 2.14 wt% C at 1150 °C (2098 °F). At room temperature it is even less, with the solubility of carbon in iron only 0.005%. Thus, the solubility of carbon in fcc iron is approximately 100 times greater than in bcc ferrite. This is a result of the fcc interstitial positions being larger, and therefore the strains imposed on the surrounding iron lattice are much lower. Even though present in very small amounts, carbon significantly influences the mechanical properties of ferrite.

Steels contain carbon in the form of cementite, while cast irons can contain either cementite or carbon in the form of graphite. Graphite is a more stable carbon-rich phase than cementite. Graphite formation is promoted by a higher carbon content and the presence of large amounts of certain alloying additions, in particular silicon. Therefore, graphite is an important phase in cast irons but is rarely found in steels. Cementite is metastable and will remain a compound at room temperature indefinitely. However, if it is heated to 650 to 705 °C (1200 to 1300 °F) for several years, it will gradually transform into iron and graphite. When graphite does form, the solubility limits and temperature ranges of phase stability are changed slightly, as indicated by the dashed lines in Fig. 8.2.

In ferrous alloys, iron is the prime alloying element, but carbon and other alloying elements are frequently used. Based on carbon content, there are three types of ferrous alloys: irons, steels, and cast irons. Commercially pure iron contains less than 0.008 wt% C and is composed almost exclusively of ferrite when it cools to room temperature. In steels, which have carbon contents in the range of 0.008 to 2 wt%, the microstructure consists of ferrite and cementite when they are slowly cooled to room temperature. Although a steel may contain as much as 2 wt% C, carbon contents are usually restricted to 1.5 wt% or less because of excessive brittleness. Generally, the carbon content is kept low in steels that require high ductility, high toughness, and good weldability, but is used at higher levels in steels that require high strength, high hardness, fatigue resistance, and wear resistance. Cast irons are classified as those alloys that contain between 2 to 6.70 wt% C; however, most cast irons contain 2 to 4 wt% C.

8.1.1 Ferrite

Ferrite is usually present in steels as a solid solution of iron containing carbon or one or more alloying elements such as silicon, chromium, manganese, and nickel. Carbon is an interstitial element, while the larger elements are substitutional. Carbon occupies specific interstitial sites in the bcc iron crystalline lattice, while the larger substitutional elements replace or substitute for iron atoms. The two types of solid solutions impart different characteristics. For example, interstitial carbon can easily diffuse

through the open bcc lattice, whereas substitutional elements diffuse much more slowly. Therefore, carbon responds quickly during heat treatment, whereas substitutional alloying elements behave more sluggishly. Interstitial alloying elements have a much stronger influence on the properties of iron than substitutional alloying elements. Even a small addition of carbon, less than its solubility limit, into pure iron substantially increases the room-temperature yield strength of the material (Fig. 8.3).

The influence of alloying elements on the yield strength of ferrite is shown in Fig. 8.4. The strong effects of the interstitial elements carbon and nitrogen, as well as phosphorous, are clearly evident. On the other hand, the substitutional solid-solution elements silicon, copper, manganese, molybdenum, nickel, aluminum, and chromium are far less effective as

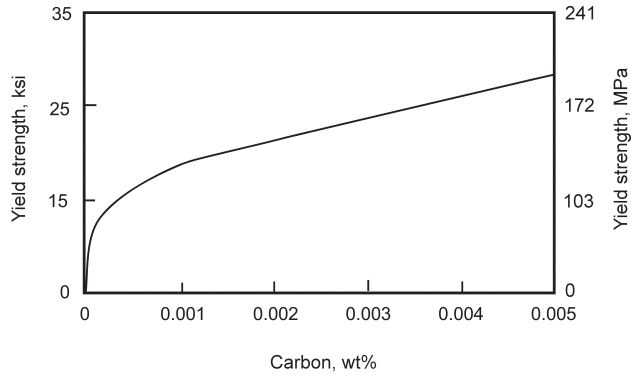

Fig. 8.3 Effect of small carbon additions on strength of iron. Source: Ref 8.4 as published in Ref 8.3

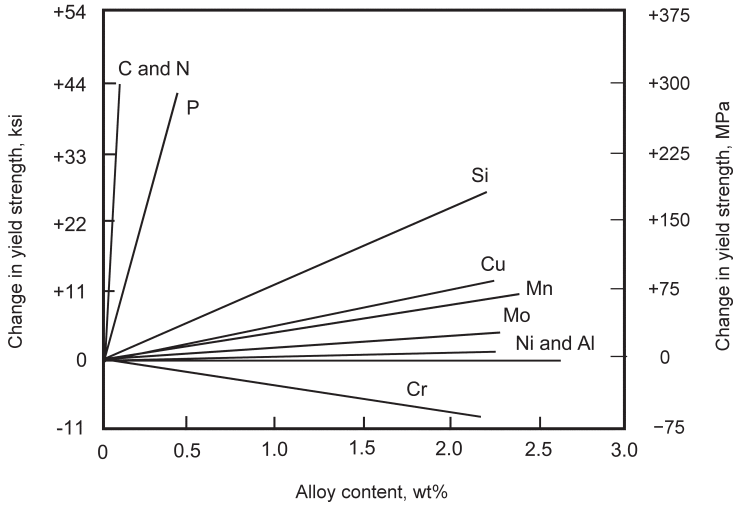

Fig. 8.4 Effect of alloying elements on yield strength. Source: Ref 8.4 as published in Ref 8.3

ferrite strengtheners. The strength of a ferritic steel is also determined by its grain size according to the Hall-Petch relationship, as shown in Fig. 8.5; that is, a finer grain size results in a higher yield strength. Control of the grain size through thermomechanical treatments, heat treatments, and/or alloying is vital to the control of strength and toughness of most steels. While a wide variety of steels contain ferrite, only a few commercial steels are totally ferritic. An example of the microstructure of a fully ferritic ultralow-carbon steel is shown in Fig. 8.6.

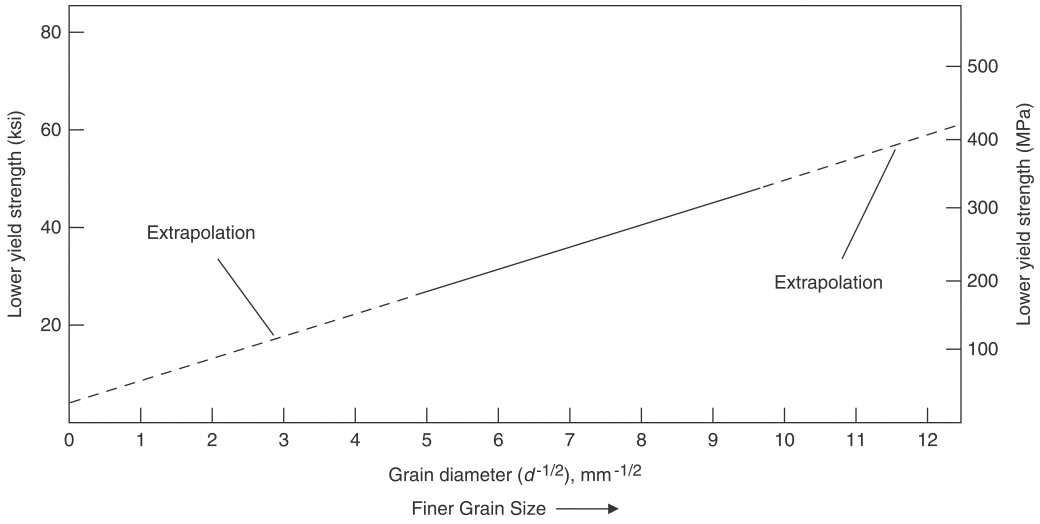

Fig. 8.5 Hall-Petch relationship for low-carbon ferritic steel. Source: Ref 8.3

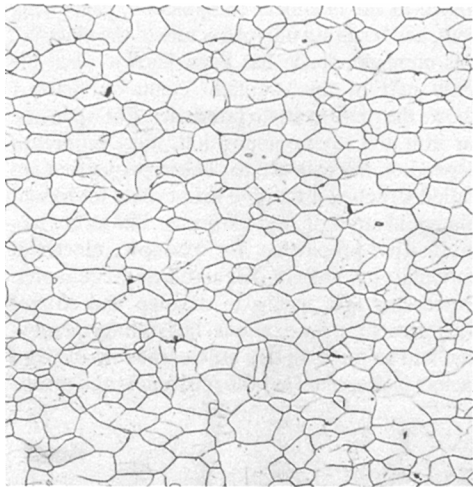

Fig. 8.6 Microstructure of ultralow-carbon ferritic steel. Source: Ref 8.4 as published in Ref 8.3

8.1.2 Eutectoid Structures

The eutectoid reaction is defined as a single-parent phase decomposing into two different product phases through a diffusional mechanism. When a steel with the eutectoid composition (0.76 wt% C) is slowly cooled through the eutectoid temperature of 725 °C (1341 °F), austenite decomposes into ferrite and cementite, in the manner shown in Fig. 8.7:

γ-austenite (0.76 wt% C) → α-ferrite (0.22 wt% C) + Fe_3C-cementite (6.7 wt% C)

At a temperature of 999 °C (1830 °F), a phase analysis of an alloy containing the eutectoid composition (0.8% C) gives:

Point: 0.8% C alloy at 1000 °C (1830 °F)	
Phase	Austenite (γ)
Composition	0.8% C
Amount	100%

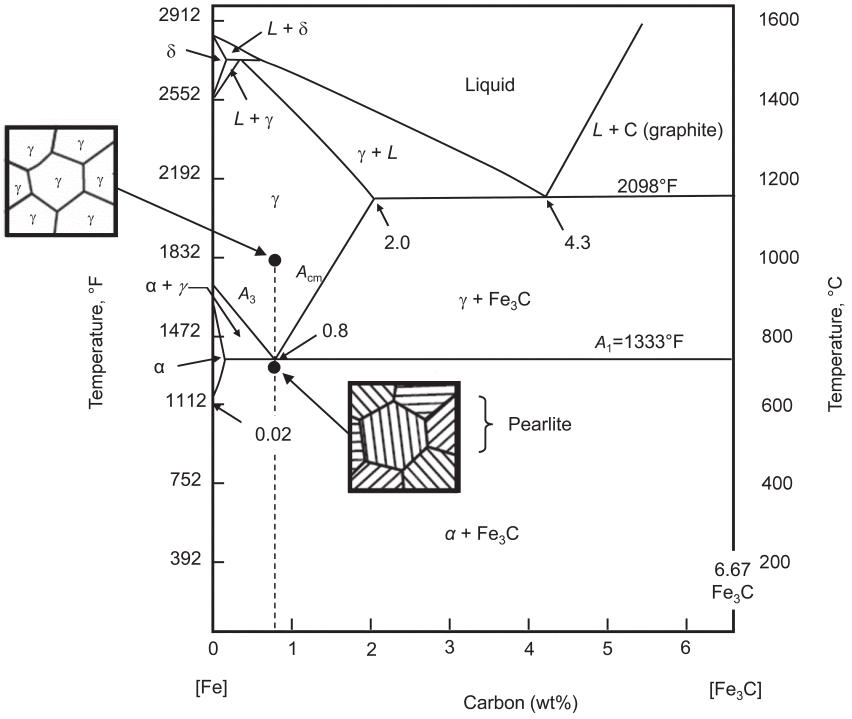

Fig. 8.7 Equilibrium cooling of a eutectoid steel. δ-ferrite, bcc; γ-austenite, fcc; α-ferrite, bcc; Fe3C, cementite. Source: Ref 8.3

When the alloy is cooled past the eutectoid temperature (720 °C, or 1333 °F), ferrite and cementite form side by side within the austenite to create a nodule of pearlite, the eutectoid microconstituent. A phase analysis just below the eutectoid temperature reveals:

Point: 0.8% C at 700 °C (1290 °F)		
Phases	Ferrite (α)	Cementite (Fe_3C)
Compositions	0.3% C	6.7% Fe_3C
Amounts	100% – 12% ≈ 88%	$\text{wt\%}Fe_3C = \frac{0.80 - 0.03}{6.7 - 0.03} \approx 12\%$

Because the corresponding microstructure is 100% pearlite, it follows that pearlite consists of 88% ferrite and 12% cementite. Pearlite is a lamellar construction consisting of alternating layers of ferrite and cementite. As shown in Fig. 8.8, either ferrite or cementite nuclei form at austenite grain boundaries and then grow as colonies into the austenite grains, with the layers oriented in essentially the same direction within the colony. The concurrent growth of several colonies leads to the formation of a larger nodule. The interface between the growing pearlite and austenite is incoherent. Provided that the temperature is constant, pearlite advances at a constant velocity and tends to produce a hemispherical nodule. The mechanism of pearlite growth involves the rejection of carbon by the growing ferrite plates and its incorporation into the cementite. This process requires diffusion of carbon by one or more of three paths: through the austenite, through the ferrite, or along the interface. The lower the transformation

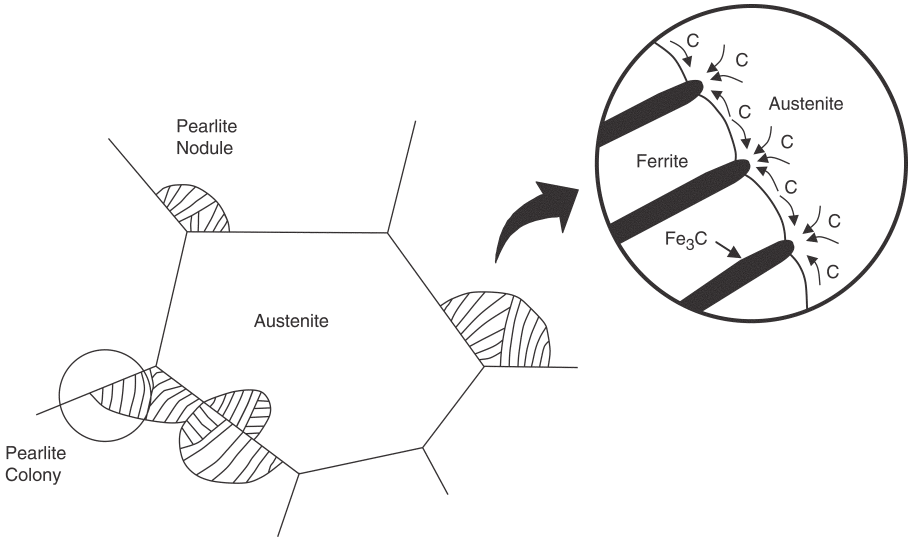

Fig. 8.8 Formation of pearlite from austenite. Source: Ref 8.5 as published in Ref 8.3

temperature, the greater is the chemical energy driving the reaction, resulting in a finer pearlite size. Pearlite gets its name because its appearance at low magnification under a light microscope resembles mother-of-pearl (Fig. 8.9).

The alternating α-ferrite and Fe_3C layers in pearlite form because the carbon content of the austenite parent phase (0.76 wt% C) is different from that of both ferrite (0.022 wt% C) and cementite (6.7 wt% C), and the phase transformation requires that there be a redistribution of the carbon by diffusion. Carbon atoms diffuse away from the ferrite regions to the cementite layers as the pearlite extends from the grain boundary into the austenite grains. The relative layer thickness of the eutectoid ferrite-to-cementite layers is approximately 8 to 1, meaning that the ferrite layers are a lot thicker than the cementite layers. When the rate of cooling is slow enough for the transformation to begin and end just below the eutectoid isotherm, the product will be coarse pearlite. As the cooling rate increases, pearlite with increasingly fine structure will develop.

Although energy minimization would normally predict a structure of dispersed spheroids, the alternating platelet structure forms because the carbon diffuses a shorter distance than is required to form a dispersed spheroid microstructure. Diffusion is possible because the small interstitial carbon atoms can diffuse quite rapidly through the iron lattice at elevated

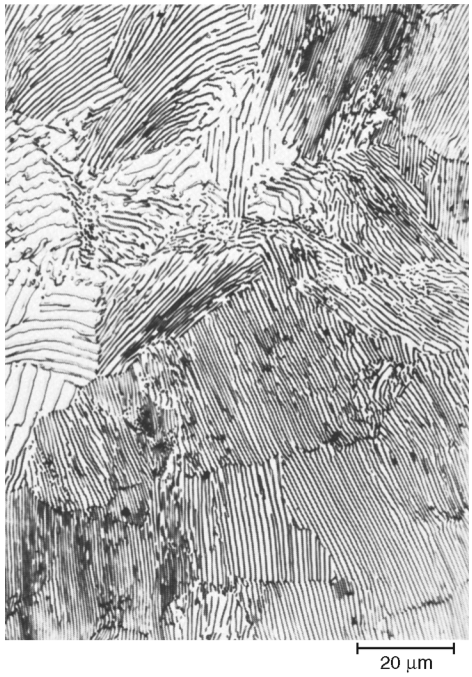

Fig. 8.9 Pearlitic structure in eutectoid steel. Source: Ref 8.6 as published in Ref 8.3

temperatures. In addition, diffusion is faster in the more loosely packed bcc ferrite structure than the closer packed fcc austenite structure. However, diffusion in solids during a eutectoid reaction is much slower than in liquids during the eutectic reaction. Therefore, nonequilibrium transformations are even more important in eutectoid solid-state reactions than in the liquid-to-solid eutectic reactions. Subsequent cooling of pearlite from the eutectoid to room temperature produces only insignificant changes in the microstructure.

The morphology of a pearlite nodule is illustrated Fig. 8.10. Pearlite nodules nucleate at prior austenite grain boundaries and triple points to minimize the free energy needed for the transformation. Each nodule contains sub-units (colonies) of cementite and ferrite lamellae; each colony has a specific orientation relation with the parent austenite grain. Pearlite nucleation occurs when either ferrite or cementite nucleates on a heterogeneity in the parent structure, such as the austenite (or parent phase) grain boundaries or grain-boundary triple points. The selection of which phase nucleates is determined by the orientation and local composition. For the case of cementite, which is orthorhombic, the relationship between the newly formed cementite and the parent austenite is:

$$(100)_c \| (1\bar{1}1)_\gamma, (0\bar{1}0)_c \| (110)_\gamma, (001)_c \| (\bar{1}12)_\gamma$$

This creates a low-mobility semicoherent interface with the grain, γ_1, with which the orientation relation was developed, and a high-mobility incoherent interface with austenite grain, γ_2, in Fig. 8.11(a). Thus, the newly formed pearlite colony grows by the high-mobility incoherent interface expanding

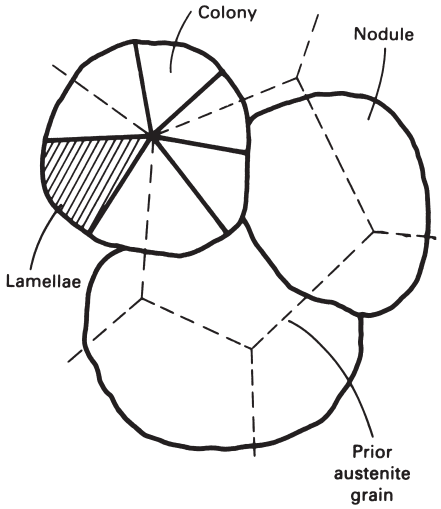

Fig. 8.10 Relationship of pearlite lamellae, colonies, and nodules to prior austenite grains. Source: Ref 8.7 as published in Ref 8.1

into the austenite grain with which the pearlite does not have an orientation relationship. The nucleation of this cementite creates a "carbon-free" region around it, promoting the nucleation of ferrite on both sides of the cementite. The interface between the newly formed cementite and ferrite is semicoherent as well, which promotes lamellae lengthening through the higher-mobility incoherent interface between the lamellae and the parent austenite, rather than lamellae spacing coarsening. This causes the colony shape to become radial from the point of original nucleation as existing lamellae lengthen into the austenite and new lamellae nucleate at the edges (Fig. 8.11b–c and 8.12). This semicoherent interface in a commercial steel is illustrated in Fig. 8.13 and 8.14. Thus, the pearlite colony grows by the incoherent interface expanding into grain γ_2 (Fig. 8.11a, part 4). This growth occurs by a ledge-growth mechanism (Fig. 8.15). This cooperative nucleation and growth is key to the development of the pearlite morphology. This cooperative growth is dependent on both diffusion of carbon

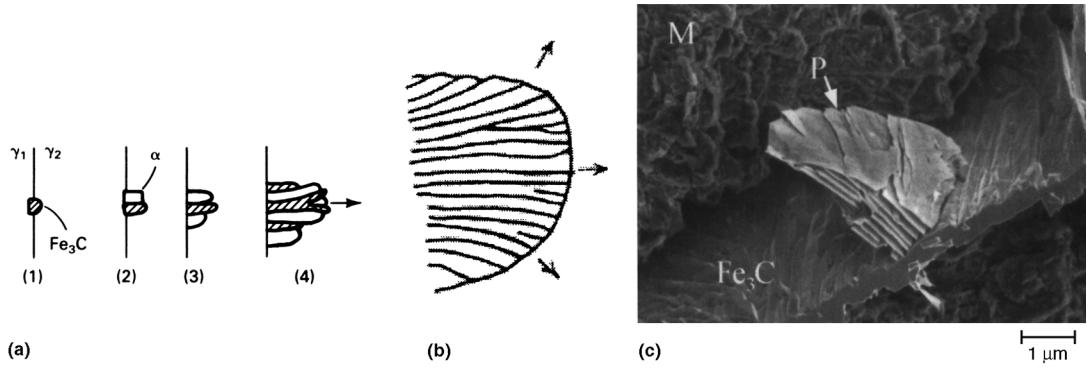

Fig. 8.11 (a) Pearlite nucleation. (b) Colony growth. (c) Deep-etched steel sample showing pearlite colony growth from a proeutectoid cementite plate. Source: Ref 8.8 as published in Ref 8.1

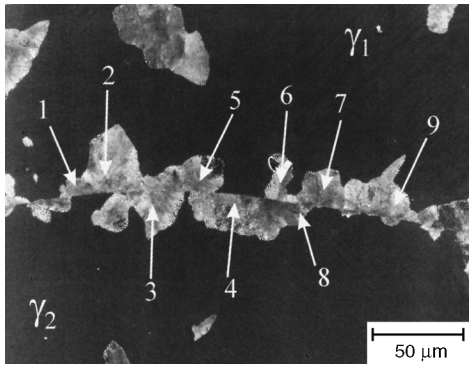

Fig. 8.12 Growth of intergranular pearlite nodules (numbered light regions) into the austenite matrix (dark). Source: Ref 8.9 as published in Ref 8.1

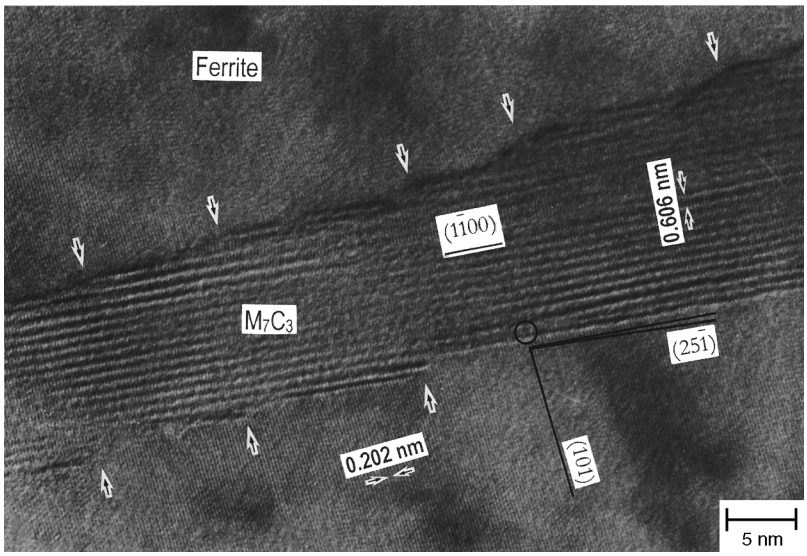

Fig. 8.13 High-resolution electron micrograph of two ferrite regions split by a carbon-rich M_7C_3 lamellae in an Fe-8.2Cr-0.92C alloy. Source: Ref 8.10 as published in Ref 8.1

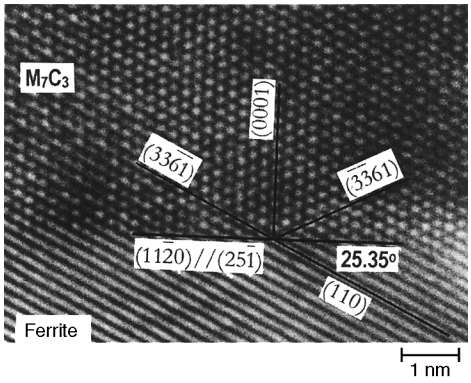

Fig. 8.14 Interface between M_7C_3 and ferrite seen in Fig. 8.13. The interface is semicoherent, pinning any movement. Source: Ref 8.10 as published in Ref 8.1

as well as structural sharing of growth ledges between the cementite and ferrite (Fig. 8.16).

If the ferrite nucleates first, it forms an orientation relation with γ_1 that is close to the Kurdjumov-Sachs relation:

$$\{110\}_f \| \{111\}_\gamma \langle 1\bar{1}1\rangle_f \| \langle 1\bar{1}0\rangle_\gamma$$

Carbon is rejected into the austenite, promoting the nucleation of cementite. The pearlite colony grows into the austenite grain with which it does

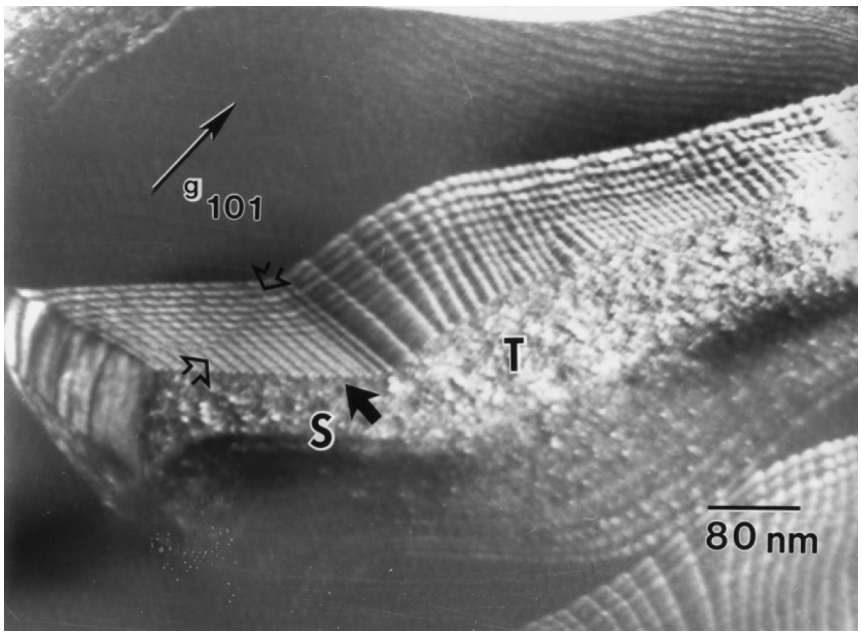

Fig. 8.15 Dark-field ferrite growth front illustrating ledge growth. Source: Ref 8.1

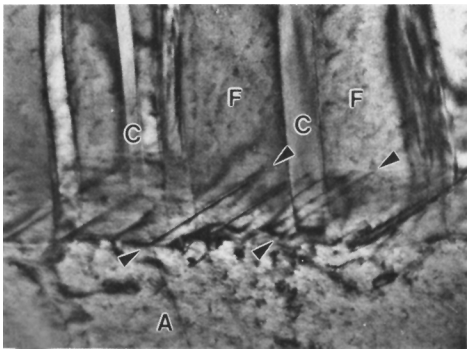

Fig. 8.16 Growth front of pearlite indicating that ledges span both cementite (C) and ferrite (F) as they grow into the austenite (A). Source: Ref 8.11 as published in Ref 8.1

not have the orientation relationship due to the relative ease of moving the high-energy incoherent interface.

The growth rate of pearlite is best represented by the Johnson-Mehl-Avrami equation:

$$f = 1 - \exp(-kt^n)$$

where f is fraction transformed, k accounts for the growth and nucleation rates, t is time, and n is the Avrami exponent. The exponent n varies from

1 to 4, where 1 represents a needle-shaped precipitate and 4 represents a spherical precipitate. The k factor can be rewritten as:

$$k = k_0 \exp\left[\frac{-Q}{RT}\right]$$

where k_0 is a constant, Q is the activation energy, R is the universal gas constant, and T is the temperature. Thus, the growth rate is very dependent on temperature, particle shape, and time. Figure 8.17 illustrates this with a time-temperature-transformation (TTT) diagram showing the time for transformation at two different temperatures. It is seen that the fraction transformed curve is sigmoidal. The initial rate is slow due to relatively few nodules existing. The rate increases with the nucleation rate until nodule impingement, when the transformation rate slows to completion. The C-curve nature of the TTT diagram in Fig. 8.17(a) shows that transformation times are slow at both temperatures close to (small undercooling) and far from (large undercooling) the reaction temperature. This can be explained by the small amount of driving force for nucleation at small undercoolings and very slow diffusion rates at large undercoolings. The intermediate temperatures (approximately temperature T_2 in Fig. 8.17a, corresponding to the "nose" of the C curve), provide an optimal combination of nucleation driving force and diffusion rates for the fastest transformation rate.

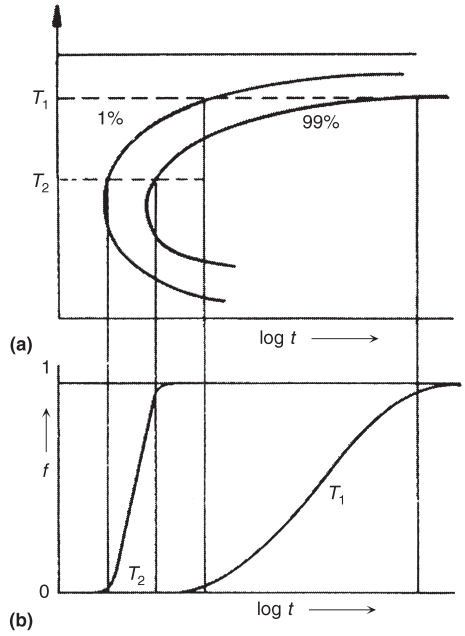

Fig. 8.17 (a) Time-temperature-transformation diagram indicating two temperatures. (b) Time required for transformation as a function of temperature. Source: Ref 8.12 as published in Ref 8.1

The lamellar spacing of the pearlite structure gives an indication of the transformation temperature. As the transformation temperature decreases, the diffusivity of carbon in austenite decreases, which acts to limit the interlamellar spacing. The variation of pearlite spacing versus transformation temperature for steel is shown in Fig. 8.18. The properties of fully pearlitic steels are determined by the interlamellar spacing. A relationship similar to the Hall-Petch relationship for grain size also exists for the interlaminar spacing in pearlite, with a smaller interlaminar spacing producing a higher yield strength. Thus, strength is related to interlamellar spacing, pearlite colony size, and prior austenite grain size, with finer sizes giving better properties. The thickness of the cementite lamellae can also influence the properties of pearlite. Fine cementite lamellae can be deformed, as compared with coarse lamellae which tend to crack during deformation.

Although fully pearlitic steels with a lamellar microstructure have high strength, high hardness, and good wear resistance, they also have rather poor ductility and toughness. For example, a low-carbon, fully ferritic steel will typically have a total elongation of more than 50%, whereas a fully pearlitic steel will typically have a total elongation of only approximately 10%. A low-carbon fully ferritic steel will have a room temperature Charpy V-notch impact energy of approximately 200 J (150 ft · lbf), whereas a fully pearlitic steel will have room-temperature impact energy of under

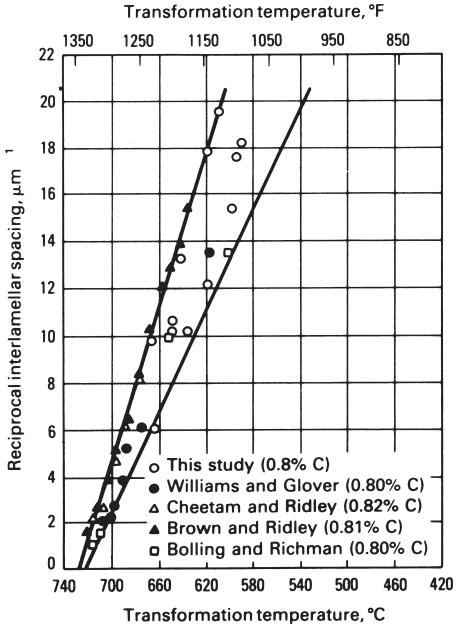

Fig. 8.18 Pearlite interlamellar spacing versus transformation temperature. Source: Ref 8.13 as published in Ref 8.1

10 J (7 ft · lbf). In addition, the transition temperature of a fully pearlitic steel is always well above room temperature. This means that at room temperature, the general fracture mode is the brittle fracture mode cleavage. Therefore, fully pearlitic steels with lamellar microstructure should not be used in applications where toughness is important. Also, pearlitic steels with carbon contents slightly or moderately higher than the eutectoid composition (i.e., hypereutectoid steels) have even lower toughness. Because of their low ductility/toughness, there are only a few applications for fully pearlitic steels, examples being railroad rails and wheels and high-strength wire. A fully pearlitic rail steel provides excellent wear resistance during railroad wheel-rail contact.

8.1.3 Hypoeutectoid and Hypereutectoid Structures

Hypoeutectoid, meaning compositions with carbon content less than the eutectoid, alloys contain 0.022 to 0.76 wt% C. Cooling of a hypoeutectoid alloy is represented by the vertical line in the Fig. 8.19 phase diagram. After solidification, at high temperatures, such as point *a*, the alloy is in the single-phase austenite field and is entirely austenite. When the alloy is cooled to approximately 800 °C (1475 °F) (point *b*), the alloy enters the two-phase $\alpha + \gamma$ phase field. Small particles of ferrite start forming along the austenite grain boundaries. This ferrite is called proeutectoid ferrite because it forms prior to cooling through the eutectoid temperature. This is in contrast to the eutectoid ferrite that forms at the eutectoid temperature as part of the constituent pearlite. While cooling the alloy through the $\alpha + \gamma$ phase region, the composition of the ferrite phase changes with temperature along the α-$(\alpha + \gamma)$ phase boundary, line *pr*, and becomes slightly richer in carbon. The change in composition of the austenite is more drastic, proceeding along the $(\alpha + \gamma)$-γ boundary, line *pq*, as the temperature is reduced. As the alloy further cools within the $\alpha + \gamma$ field (point *c*), the ferrite particles become larger in size and thicken along the austenite grain boundaries. When the alloy is finally cooled through the eutectoid temperature (point *d*), all of the remaining austenite transforms to pearlite. Because this reaction does not really affect the proeutectoid ferrite that has already formed at the austenite grain boundaries, the final microstructure is one of pearlite within the grain interiors surrounded by proeutectoid ferrite at the prior austenite grain boundaries.

The microstructure of a hypoeutectoid steel depends on how rapidly it is cooled from the austenitic phase region. Very slow cooling, such as furnace cooling, will result in the formation of proeutectoid ferrite at the austenite grain boundaries. The remaining austenite grains will then convert to pearlite as the steel cools through the eutectoid temperature. As the temperature decreases, the morphology of proeutectoid ferrite changes. Growth along the grain boundaries becomes markedly easier than growth normal to them. Therefore, films of proeutectoid ferrite form at the sites

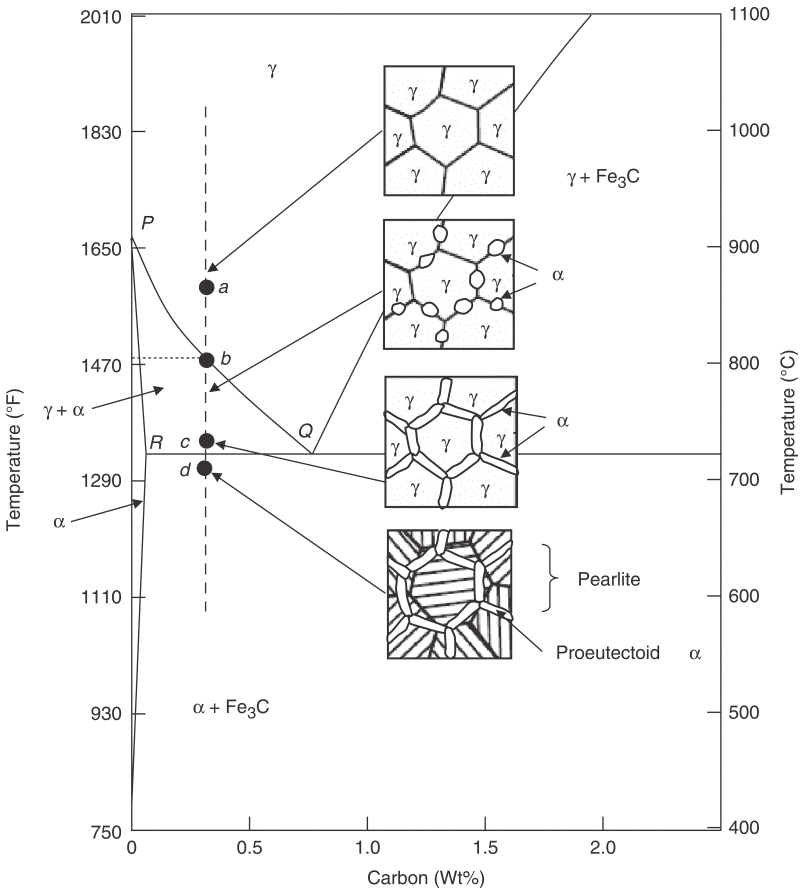

Fig. 8.19 Equilibrium cooling of a proeutectoid steel. Source: Ref 8.3

of the former austenite boundaries. If the cooling rate is fast, ferrite side-plates protrude from the proeutectoid ferrite and project into the austenite grains. These side-plates, called Widmanstätten plates, have a wedge-like shape, and their broad faces comprise flat areas separated by ledges (Fig. 8.20). The growth process now involves the nucleation and sideways migration of the ledges that separate the flats. Thus, the microstructure of hypoeutectoid steel that is cooled rapidly will contain Widmanstätten ferrite and fine pearlite.

The transformations of hypereutectoid steels, those containing 0.077 to 2 wt% C, is exactly analogous to hypoeutectoid steels, except that in this instance, proeutectoid cementite forms on the grain boundaries in the manner shown in the Fig. 8.21 phase diagram. This phase diagram also illustrates why hypereutectoid steels are only used where extreme hardness is required, such as in cutting tools. Note that the cementite forms a continuous network along the prior austenite grain boundaries. Because

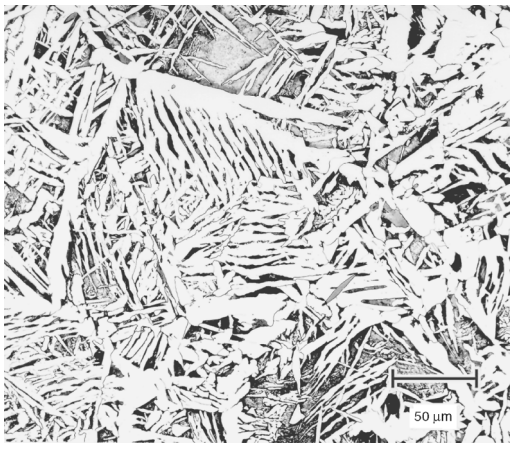

Fig. 8.20 Widmanstätten ferrite. Source: Ref 8.14 as published in Ref 8.3

cementite is a hard and brittle compound, these steels have very little ductility and can be prone to sudden brittle failures. When hypereutectoid steels are fractured, it is common to find a region of the fracture that appears to be intergranular where the crack propagated along the proeutectoid cementite grain-boundary films.

Compositions below 0.77 wt% C in iron-carbon systems will nucleate proeutectoid ferrite before reaching the eutectoid temperature and formation of pearlite. This ferrite nucleates at the grain boundaries to reduce energy and follows the Kurdjumov-Sachs relationship stated previously. A pearlite colony will then grow from the proeutectoid ferrite once the eutectoid temperature has been reached.

For compositions above the eutectoid point, proeutectoid cementite nucleates at the grain boundaries. This tends to form as a layer having the Bagaryatski orientation relationship with the γ_1 austenite grain ($[100]_c \parallel [01\,\bar{1}\,1]_\gamma$, $[010]_c \parallel [1\,\bar{1}\,\bar{1}]_\gamma$, $(001)_c \parallel (211)_\gamma$). A pearlite colony will then grow from the proeutectoid cementite once the eutectoid temperature has been reached (Fig. 8.22). In this case it is seen that pearlite nucleation is not limited predominantly to the grain boundaries.

In most ferrite-pearlite steels, the carbon content and the grain size determine the microstructure and resulting properties. For example, the effect of carbon on tensile and impact properties is shown in Fig. 8.23. The ultimate tensile strength steadily increases with increasing carbon content. This is caused by the increase in the volume fraction of pearlite in the microstructure, which has much higher strength than that of ferrite. Thus, increasing the volume fraction of pearlite has a profound effect on increasing tensile strength (Fig. 8.24). However, the yield strength is relatively unaffected by carbon content, rising from approximately 280 to 420 MPa (40 to 60 ksi) over the range of carbon content shown. This occurs because yielding in a ferrite-pearlite steel is controlled by the ferrite matrix, which

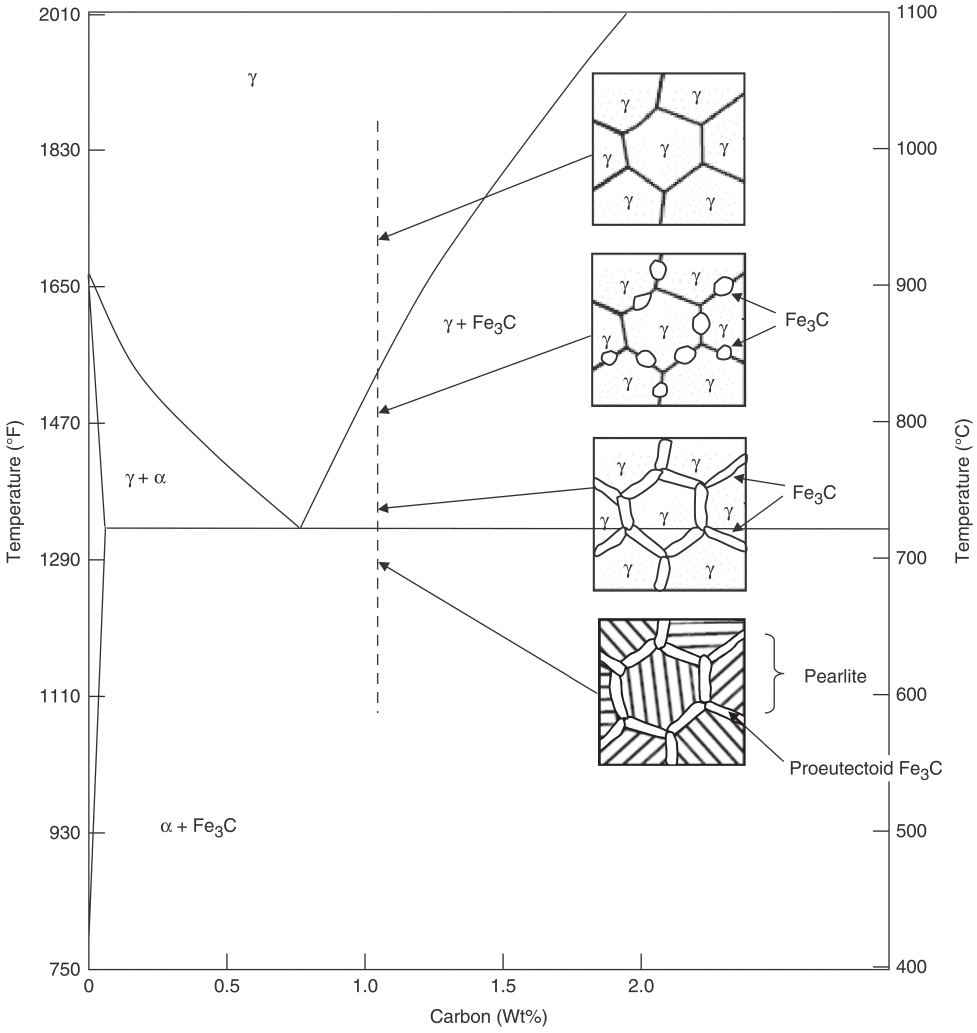

Fig. 8.21 Equilibrium cooling of a hypereutectoid steel. Source: Ref 8.3

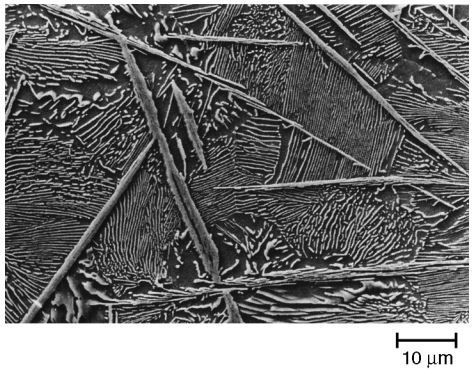

Fig. 8.22 Pearlitic microstructure with Widmanstätten cementite plates acting as nucleation sites. Source: Ref 8.11 as published in Ref 8.1

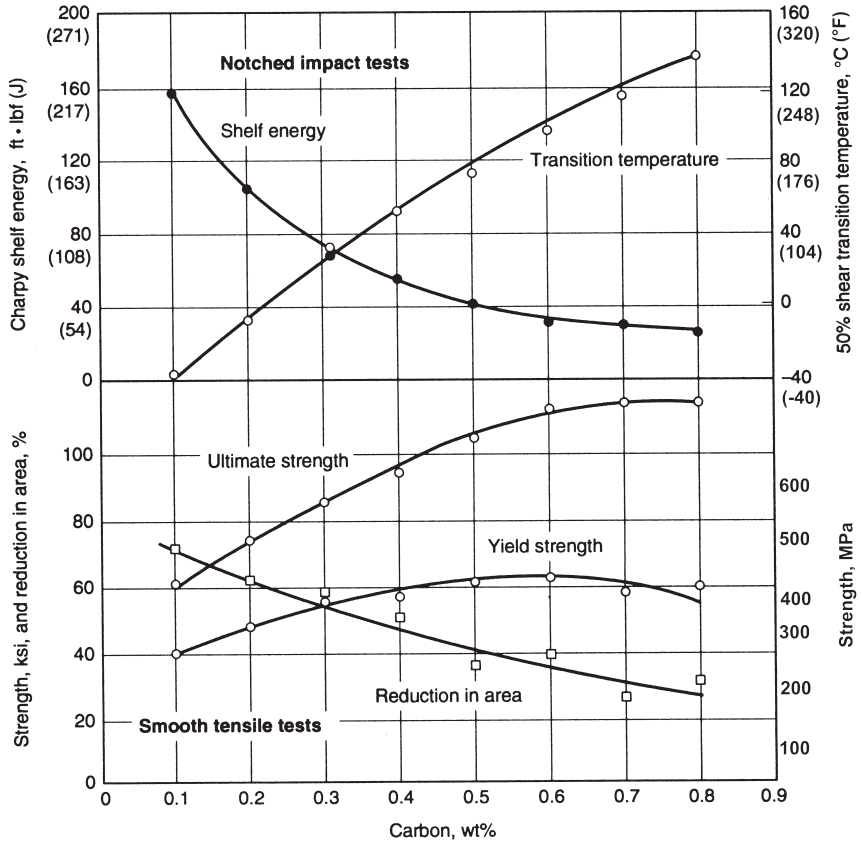

Fig. 8.23 Effects of carbon content on mechanical properties. Source: Ref 8.4 as published in Ref 8.3

is generally the continuous matrix phase in the microstructure. Therefore, pearlite plays only a minor role in yielding behavior. Ductility, as represented by reduction in area, steadily decreases with increasing carbon content. For example, a steel with 0.10 wt% C has a reduction in area of approximately 75%, whereas a steel with 0.70 wt% C has a reduction in area of only 25%.

During plastic deformation in pearlite lamellar microstructures, stress concentrations are created at the ends of pile-ups where the dislocations in the ferrite meet the ferrite-carbide interfaces, leading to carbide cracking. Cracking occurs more rapidly when the ferrite plates are thicker, because more dislocations can participate in an individual pileup for a given applied stress. The generation of cracks in cementite plates can initiate general fracture, which implies that coarse pearlite should fail before fine pearlite, because the cementite plates are expected to crack sooner when the ferrite lamellae are thicker. Also, the cracks will be longer and therefore more able to propagate. In other words, fine pearlite is both stronger and more ductile than coarse pearlite.

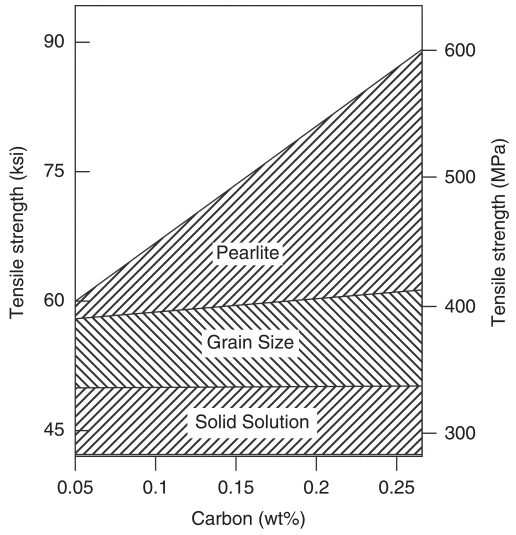

Fig. 8.24 Effect of pearlite content on mechanical properties. Source: Ref 8.15 as published in Ref 8.3

The toughness of ferrite-pearlite steels is another important consideration for applications. This is true for other bcc metals, almost all of which, unlike fcc metals, have a ductile-to-brittle transition temperature under impact loading. This is often measured by the Charpy V-notch impact test in which a notched square-section bar is broken by a swinging pendulum. Measuring the height of the pendulum at the beginning of the test and the height to which it rises after breaking the specimen enables the energy consumed in breaking the bar to be calculated. When the bar breaks in a brittle mode, the energy consumed is small. In this case, the bar breaks into two pieces and the pendulum swings onward and upward. When fracture occurs in a ductile fashion, a large amount of energy is expended by the deformation processes that precede fracture, as well as those accompanying fracture. Then, the distance traveled by the pendulum after the fracture is smaller. Extremely ductile samples may not even break, stopping the pendulum. The nature of the fracture and the amount of energy expended in an individual test can vary with the testing temperature; therefore, it is standard practice to perform Charpy tests over a range of temperatures.

It has long been known that the absorbed energy in a Charpy V-notch test decreases as the carbon content increases (Fig. 8.25). In this graph showing impact energy versus test temperature, the upper shelf energy decreases from approximately 200 J (150 ft · lbf) for a 0.11 wt% C steel to approximately 35 J (25 ft · lbf) for a 0.80 wt% C steel. Also, the transition temperature increases from approximately –50 to 150 °C (–60 to 300 °F) over this range of carbon content. The effect of carbon is due mainly to its effect on the percentage of pearlite in the microstructure. The eutectoid

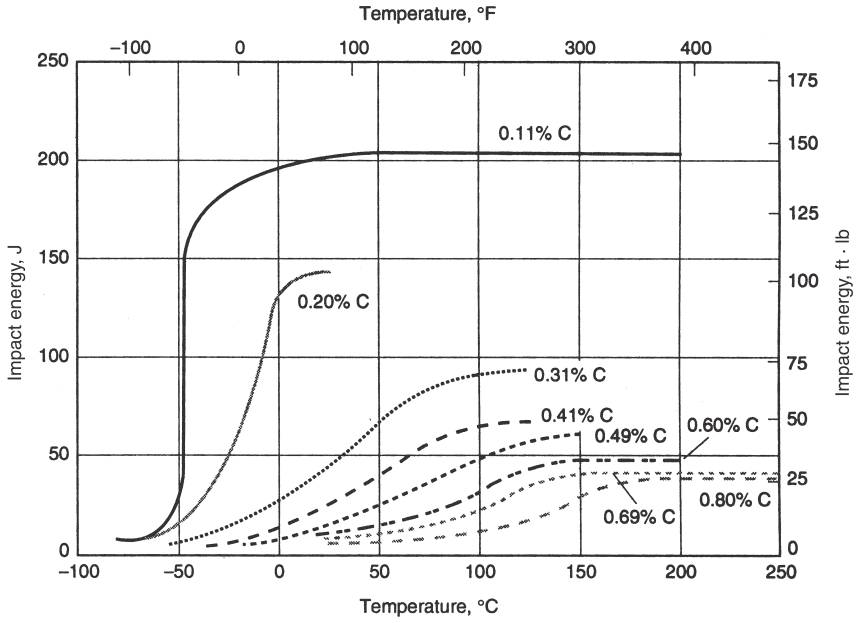

Fig. 8.25 Effect of carbon content on impact properties. Source: Ref 8.4 as published in Ref 8.3

steel, which is entirely pearlitic, shows a gradual transition of the energy consumed as a function of temperature. Presumably, the gradual transition at the high pearlite levels occurs because, even though the cementite plates crack, the total fracture path is tortuous in comparison to cleavage in the ferrite. Cleavage fracture in ferrite is a brittle fracture process in which the fracture path follows particular crystallographic planes in each grain, forming large, relatively flat facets.

Until approximately 20 years ago, hypoeutectoid steels with mixed ferrite-pearlite microstructures were commonly selected for structural applications because of their useful strength levels. Applications included beams for bridges and high-rise buildings, plates for ships, and reinforcing bars for roadways. These steels are relatively inexpensive and are produced in large tonnages. They also have the advantage of being able to be produced with a wide range of properties. Unfortunately, medium-to-high-carbon steels are not very amendable to welding and are therefore usually bolted or riveted together. In addition, their low toughness and high ductile-to-brittle transition temperatures can cause catastrophic failures. Today, high-strength low-alloy (HSLA) steels are replacing conventional hypoeutectoid steels in many structural applications. The HSLA steels, which have very low carbon contents, have an attractive combination of properties, including high strength, good toughness, a low ductile-to-brittle transition temperature, and are more readily weldable.

8.1.4 Alloying Elements

The addition of substitutional alloying elements causes the eutectoid composition and temperature to shift in the iron-carbon system. The effect of various substitutional alloying elements on the eutectoid transformation temperature and effective carbon content are shown in Fig. 8.26 and 8.27, respectively. Because the formation of pearlite is heavily dependent on long-range diffusion, the addition of these substitutional alloying elements will have a significant effect on the reaction kinetics as well. The addition of substitutional elements will decrease the diffusion rate and slow down the reaction kinetics, an effect known as partitioning and solute drag. Much like carbon, these substitutional alloying elements prefer to partition into either the ferrite or cementite lamellae of the pearlite. Because the rate of pearlite formation depends heavily on diffusion, the substitutional

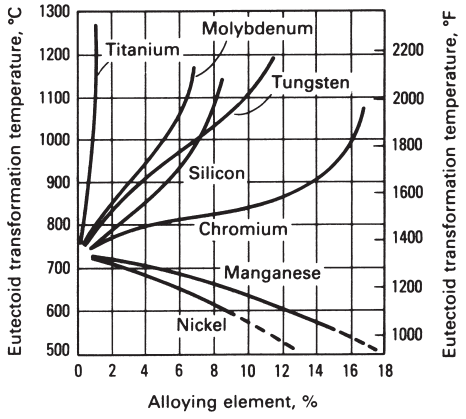

Fig. 8.26 Effect of alloying element on eutectoid temperature. Source: Ref 8.16 as published in Ref 8.1

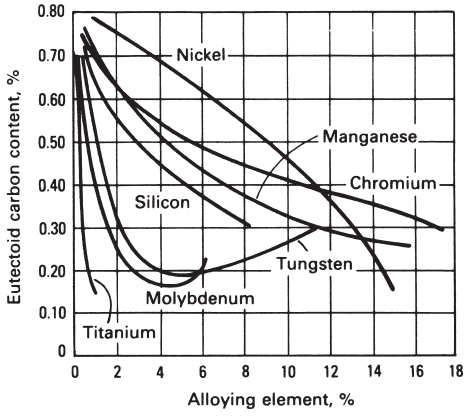

Fig. 8.27 Effect of alloying elements on effective carbon content. Source: Ref 8.16 as published in Ref 8.1

alloying elements control the rate of transformation due to substitutional diffusion being much slower than interstitial carbon diffusion. This effect is known as solute drag and can be seen by the shifting of the TTT diagram to the right, indicating increased time of reaction. The effects of alloying elements and their distribution in the pearlitic microstructure are shown in Fig. 8.28, while their effect on reaction time is evidenced by increasing reaction times in the TTT diagram (Fig. 8.29).

8.2 Peritectoid Structures

The term *peritectoid* denotes the special case of an equilibrium phase in which two or more solid phases (which are stable above the temperature T_p) react at T_p to form a new solid phase. This reaction can be written as:

$$\alpha + \beta \rightarrow \gamma$$

Peritectoid phase equilibria are very common in binary phase diagrams. Peritectoid transformations are similar to peritectic transformations, except that the initial phases are both solid. An example of a peritectoid transformation is provided by the formation of the intermetallic compound U_3Si in uranium-silicon alloys. The relevant phase diagram is shown in Fig. 8.30.

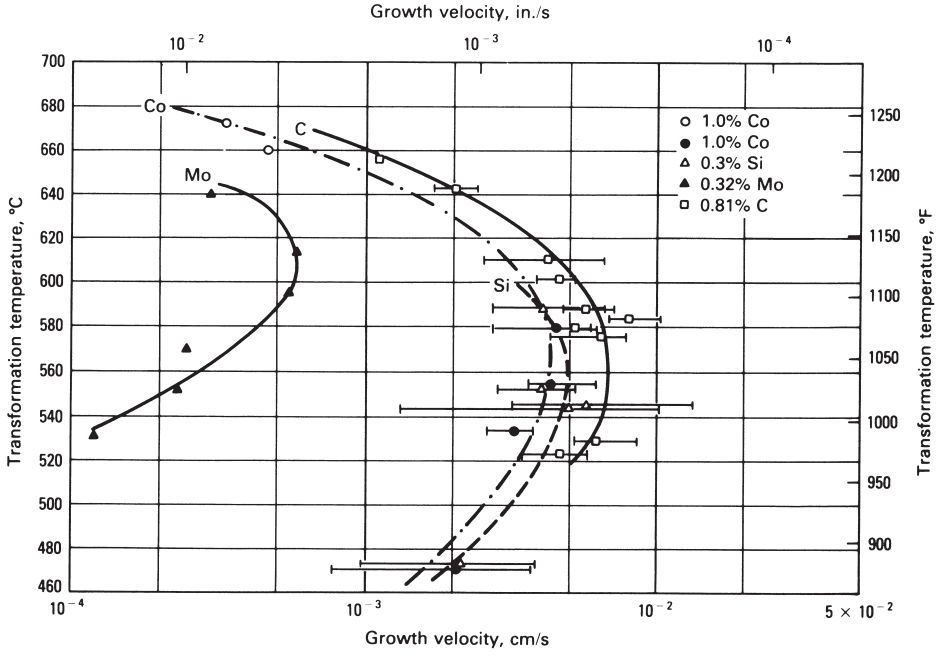

Fig. 8.28 The partitioning effect of substitutional alloying elements chromium, manganese, and silicon in pearlitic steel. Source: Ref 8.17 as published in Ref 8.1

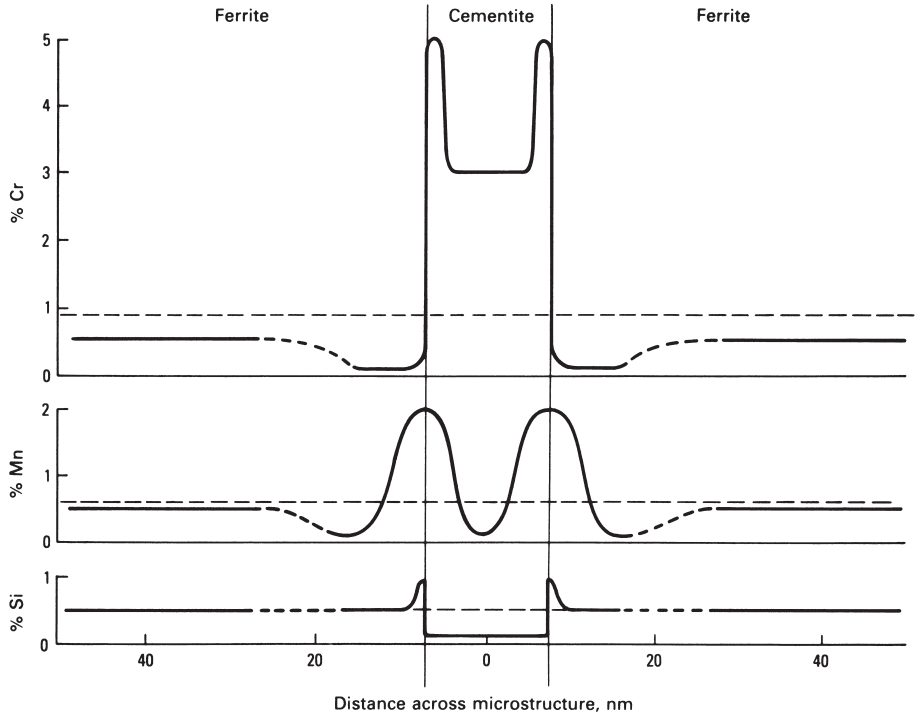

Fig. 8.29 Pearlite growth rate in Fe-C-X alloys as a function of temperature. Source: Ref 8.18 as published in Ref 8.1

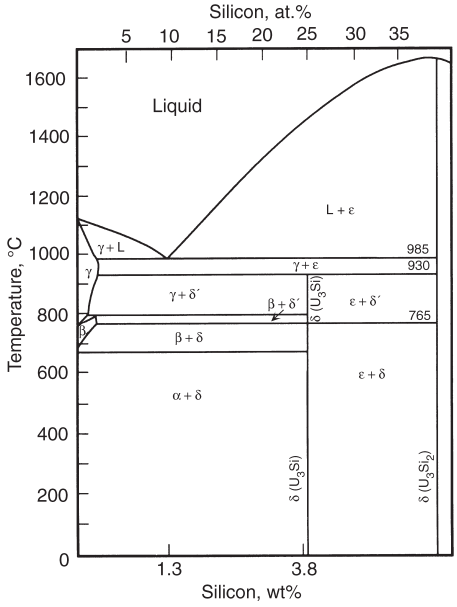

Fig. 8.30 Portion of the uranium-silicon phase diagram. Source: Ref 8.19 as published in Ref 8.1

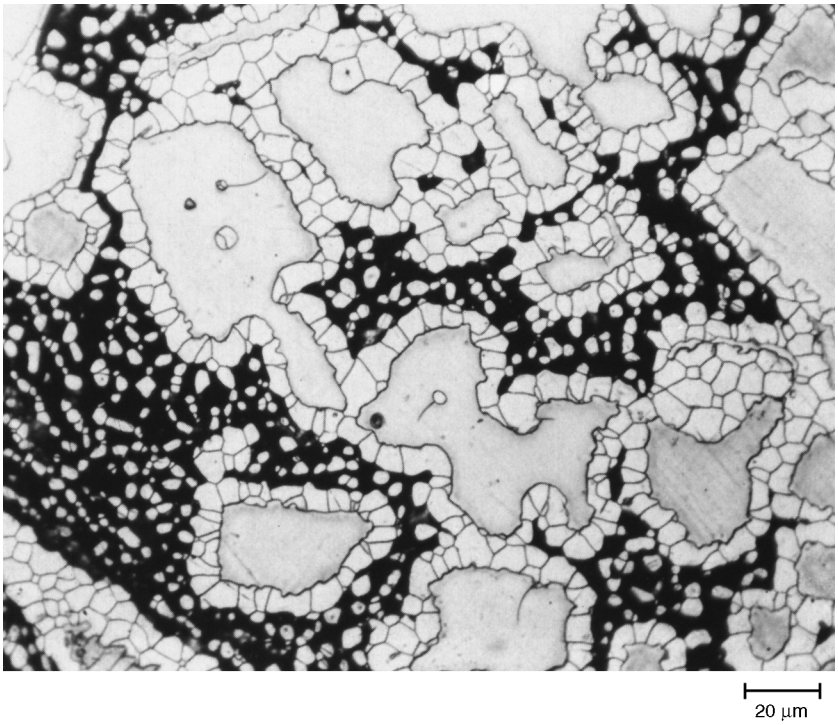

Fig. 8.31 Casting of a uranium-silicon alloy that contains 3.8% Si. Grains of U_3Si_2 are surrounded by grains of U_3Si on a background of a eutectic matrix that is a mixture of uranium and U_3Si. Original magnification: 500×. Source: Ref 8.19 as published in Ref 8.1

Casting uranium at the proper concentration of silicon (3.78%) results in a mixture of uranium and U_3Si_2. Morphologically, U_3Si_2 grains appear in a eutectic matrix, which is itself a mixture of uranium and U_3Si (Fig. 8.31). By means of thermal treatment below 930 °C (1700 °F), U_3Si grains grow at the boundary between the U_3Si_2 and the uranium phases. The reaction can be written:

$$U_3Si_2 + 3U \rightarrow 2U_3Si$$

This reaction is very slow, but when allowed to go to completion, all the material transforms to U_3Si (Fig. 8.32). The microstructure of the U_3Si phase consists mainly of transformation twins (Fig. 8.33).

ACKNOWLEDGMENT

The material for this chapter came from "Invariant Transformation Structures," in *Metallography and Microstructures,* Vol 9, *ASM Handbook*, ASM International, 2004, and *Elements of Metallurgy and Engineering Alloys* by F.C. Campbell, ASM International, 2008.

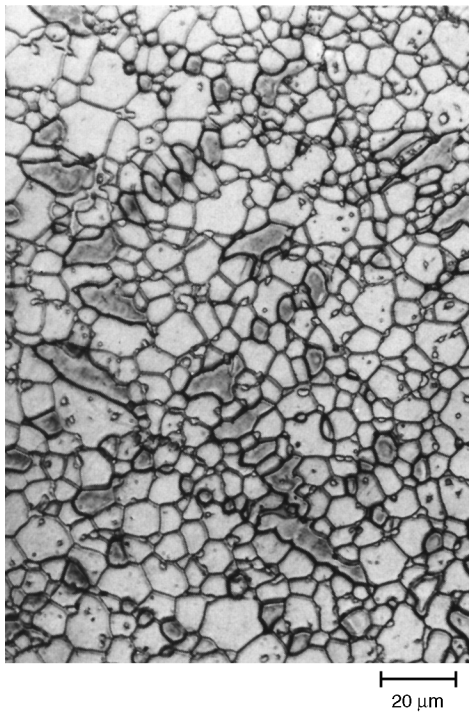

Fig. 8.32 Same uranium-silicon alloy as Fig. 8.31, but the casting has been thermally treated at 900 °C (1650 °F) for several hours. Structure is U_3Si, within which are contained the remnants of U_3Si_2. Original magnification: 500×. Source: Ref 8.1

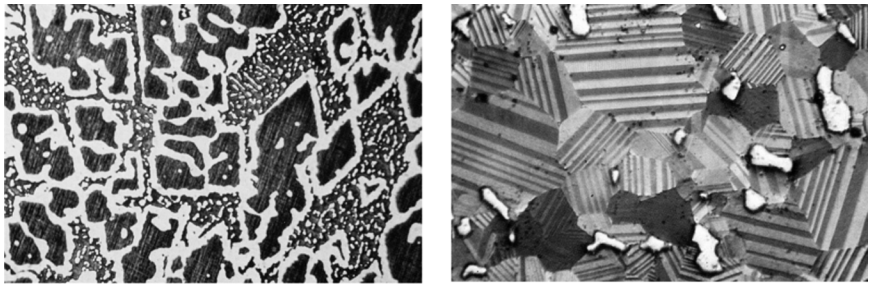

Fig. 8.33 Structure in U-3.8%Si alloy. (a) As-cast structure with U_3Si_2 (brown) surrounded by a rim of U_3Si (white) in a matrix of U-U3Si eutectic. (b) Same casting as in (a) but after heating for three days at 870 °C (1600 °F). U_3Si twinned martensite is colored; untransformed U_3Si remains uncolored. Source: Ref 8.19 as published in Ref 8.1

REFERENCES

8.1 Invariant Transformation Structures, *Metallography and Microstructures,* Vol 9, *ASM Handbook*, ASM International, 2004, p 152–164

8.2 T.B. Massalski, H. Okamoto, P.R. Subramanian, and L. Kacprzak, *Binary Alloy Phase Diagrams*, 2nd ed., ASM International, 1990

8.3 F.C. Campbell, *Elements of Metallurgy and Engineering Alloys*, ASM International, 2008

8.4 B.L. Bramfitt, Effects of Composition, Processing, and Structure on Properties of Irons and Steels, *Materials Selection and Design*, Vol 20, *ASM Handbook,* ASM International, 1997

8.5 A.G. Guy and J.R. Hren, *Elements of Physical Metallurgy*, 3rd ed., Addison-Wesley Publishing Company, 1974

8.6 D. Aliya and S. Lampman, Physical Metallurgy Concepts in Interpretation of Microstructures, *Metallography and Microstructures*, Vol 9, *ASM Handbook,* ASM International, 2004

8.7 A.R. Marder, *Phase Transformations in Ferrous Alloys,* A.R. Marder and J.I. Goldstein, Ed., TMS/AIME, 1984, p 201–236

8.8 M.A. Mangan and G.J. Shiflet, *Metall. Mater. Trans. A,* Vol 30A (No. 11), 1999, p 2767–2781

8.9 Z. Guo, T. Furuhara, and T. Maki, *Scr. Mater.,* Vol 45, 2001, p 525–532

8.10 D.V. Shtansky, K. Nakai, and Y. Ohmori, *Acta Mater.,* Vol 47 (No. 4), 1999, p 1105–1115

8.11 D.S. Zhou and G.J. Shiflet, *Metall. Trans. A,* Vol 22A (No. 6), 1991, p 1349–1365

8.12 D.A. Porter and K.E. Easterling, *Phase Transformations in Metals and Alloys,* 2nd ed., Chapman and Hall, London, 1992

8.13 A.R. Marder and B.L. Bramfitt, *Metall. Trans. A,* Vol 6, 1975, p 2009–2014

8.14 B.L. Bramfitt and S.J. Lawrence, Metallography and Microstructures of Carbon and Low-Alloy Steels, *Metallography and Microstructures*, Vol 9, *ASM Handbook,* ASM International, 2004

8.15 R.A. Higgins, *Engineering Metallurgy*, 6th ed., Arnold, 1993

8.16 E.C. Bain and H.W. Paxton, *Alloying Elements in Steel,* American Society for Metals, 1962, p 112

8.17 P.R. Williams, M.K. Miller, P.A. Beavan, and G.D.W. Smith, *Phase Transformations,* Vol 2, The Institution of Metallurgists, London, 1979, p 11.98–11.100

8.18 A.R. Marder and B.L. Bramfitt, *Metall. Trans. A,* Vol 7, 1976, p 902–906

8.19 A. Tomer, Peritectoid Transformations, *Structure of Metals Through Optical Microscopy,* ASM International, 1991